Supplement of Atmos. Chem. Phys., 25, 10949–10964, 2025
https://doi.org/10.5194/acp-25-10949-2025-supplement

Atmospheric Chemistry and Physics Open Access

Supplement of

Dry and warm conditions in Australia exacerbated by aerosol reduction in China

Jiyuan Gao et al.

Correspondence to: Yang Yang (yang.yang@nuist.edu.cn)

Table S1: Experimental design.

Experiments	Anthropogenic Emissions of Aerosols and Precursors	
	China	Other regions of the world
BASE	2013	2013
CHN	2019	2013
OTH	2013	2019
NAEU	2013	North America and Europe: 2019; Other: 2013
SASEA	2013	South Asia and Southeast Asia: 2019; Other: 2013

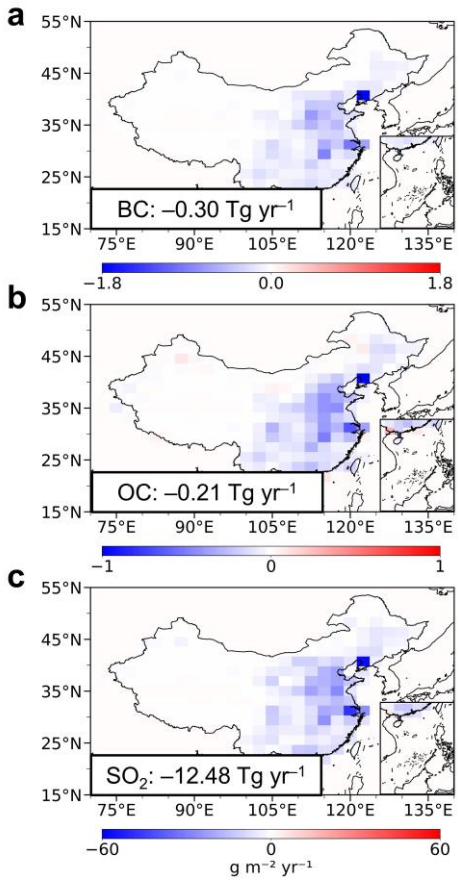

Figure S1. Differences in anthropogenic emissions of aerosols and precursors between 2013 and 2019. Spatial distributions of differences in anthropogenic emissions (unit: g m^{-2} yr^{-1}) of aerosols and precursors, including black carbon (BC, **a**), organic carbon (OC, **b**) and sulfur dioxide (SO_2, **c**) between 2013 and 2019 (2019 minus 2013). The total changes in China are noted at the bottom-left corner of each panel.

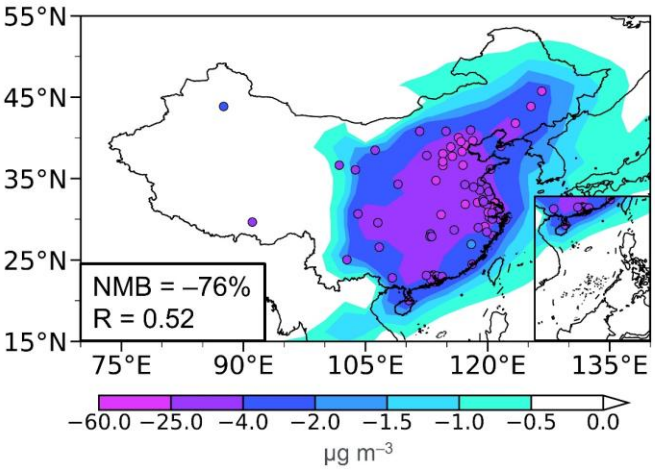

Figure S2. Comparisons of absolute changes in near-surface $PM_{2.5}$ concentrations between observation and model simulation. Spatial distributions of observed (circles) and modeled (shades) annual mean absoulte changes (2017–2019 minus 2013–2015) in near-surface $PM_{2.5}$ concentration (unit: μg m^{-3}). Normalized mean bias (NMB) and correlation coefficient (R) between observation and simulation are shown at the bottom-left corner of each panel. $NMB = 100\ \% \times \sum (Model_i - Observation_i) / \sum Observation_i$, where $Model_i$ and $Observation_i$ are the modeled and observed values at site i, respectively.

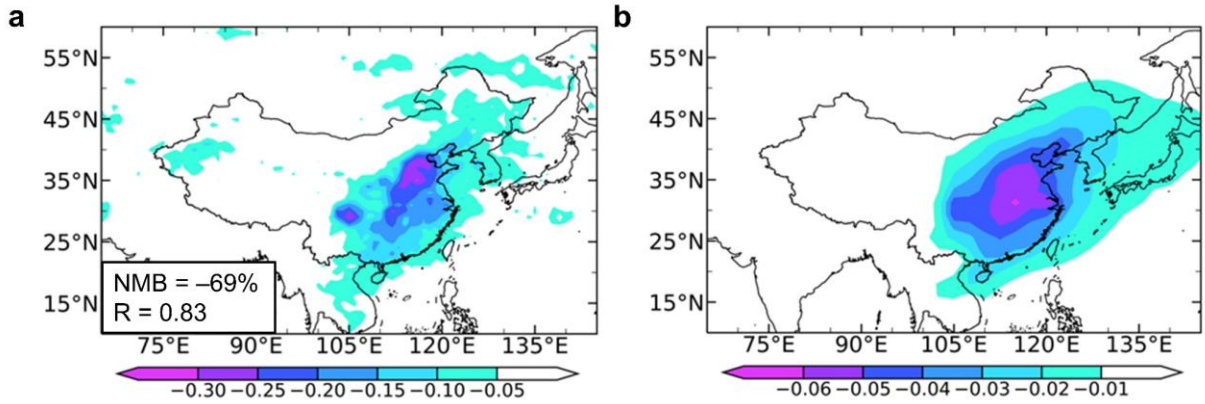

Figure S3. Comparisons of absolute changes in aerosol optical depth (AOD) between satellite retrieval and model simulation. Spatial distributions of annual mean absolute changes (2017–2019 minus 2013–2015) in Moderate Resolution Imaging Spectroradiometer (MODIS) (**a**) and modeled (**b**) AOD (unitless). Normalized mean bias (NMB) and correlation coefficient (R) between modeled AOD and MODIS AOD are shown at the bottom-left corner of panel a. $NMB = 100\ \% \times \sum (AOD\text{-}model_i - AOD\text{-}MODIS_i) / \sum AOD\text{-}MODIS_i$, where $AOD\text{-}model_i$ and $AOD\text{-}MODIS_i$ are the modeled and MODIS AOD values at grid i, respectively. Note that the magnitudes of the observed and modeled data are not directly comparable, and the color scales represent different ranges.

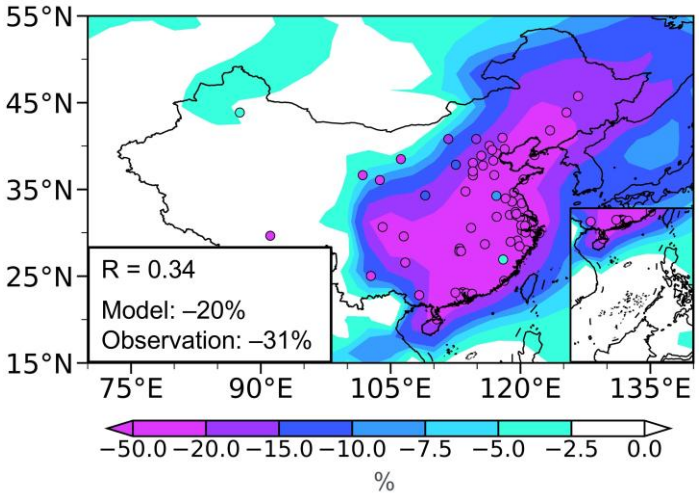

Figure S4. Comparisons of relative changes in near-surface $PM_{2.5}$ concentrations between observation and model simulation. Spatial distributions of observed (circles) and modeled (shades) annual mean relative changes (2017–2019 minus 2013–2015, relative to 2013–2015) in near-surface $PM_{2.5}$ concentration (unit: %). Relative changes of observation and model simulation and correlation coefficient (R) between observation and simulation are shown at the bottom-left corner of the panel.

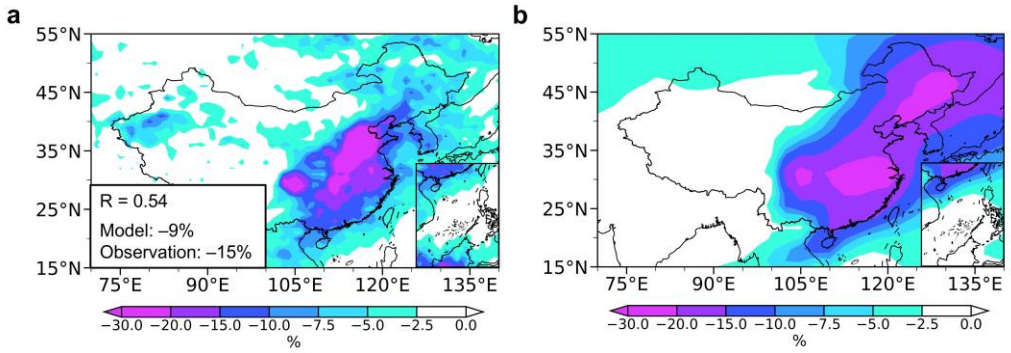

Figure S5. Comparisons of relative changes in aerosol optical depth (AOD) between satellite retrieval and model simulation. Spatial distributions of annual mean relative changes (2017–2019 minus 2013–2015, relative to 2013–2015) in Moderate Resolution Imaging Spectroradiometer (MODIS) (**a**) and modeled (**b**) AOD (unit: %). Relative changes of observation and model simulation and correlation coefficient (R) between observation and simulation are shown at the bottom-left corner of panel a.

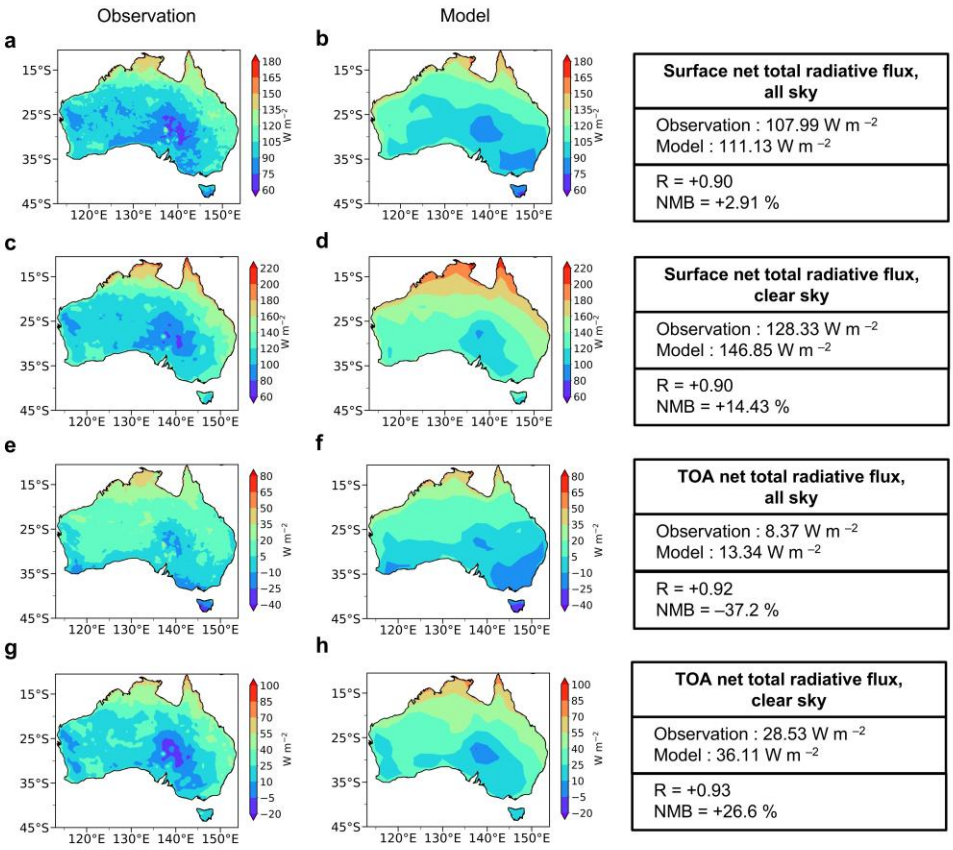

Figure S6. Comparisons of surface and TOA net total radiative flux under all sky and clear sky conditions between observation and model simulation. Spatial distributions of surface (**a**–**d**) and TOA (**e**–**h**) net total radiative flux (unit: W m^{-2}) under all sky (**a**, **b**, **e**, and **f**) and clear sky (**c**, **d**, **g**, and **h**) conditions over Australia in observation (2010–2019 annual averages from ERA5, **a**, **c**, **e**, and **g**) and model simulation (annual averages from the BASE experiment, **b**, **d**, **f**, and **h**). Regional averages over Australia in observation and model simulation and normalized mean bias (NMB) and correlation coefficient (R) between observation and model simulation are shown in the right boxes.

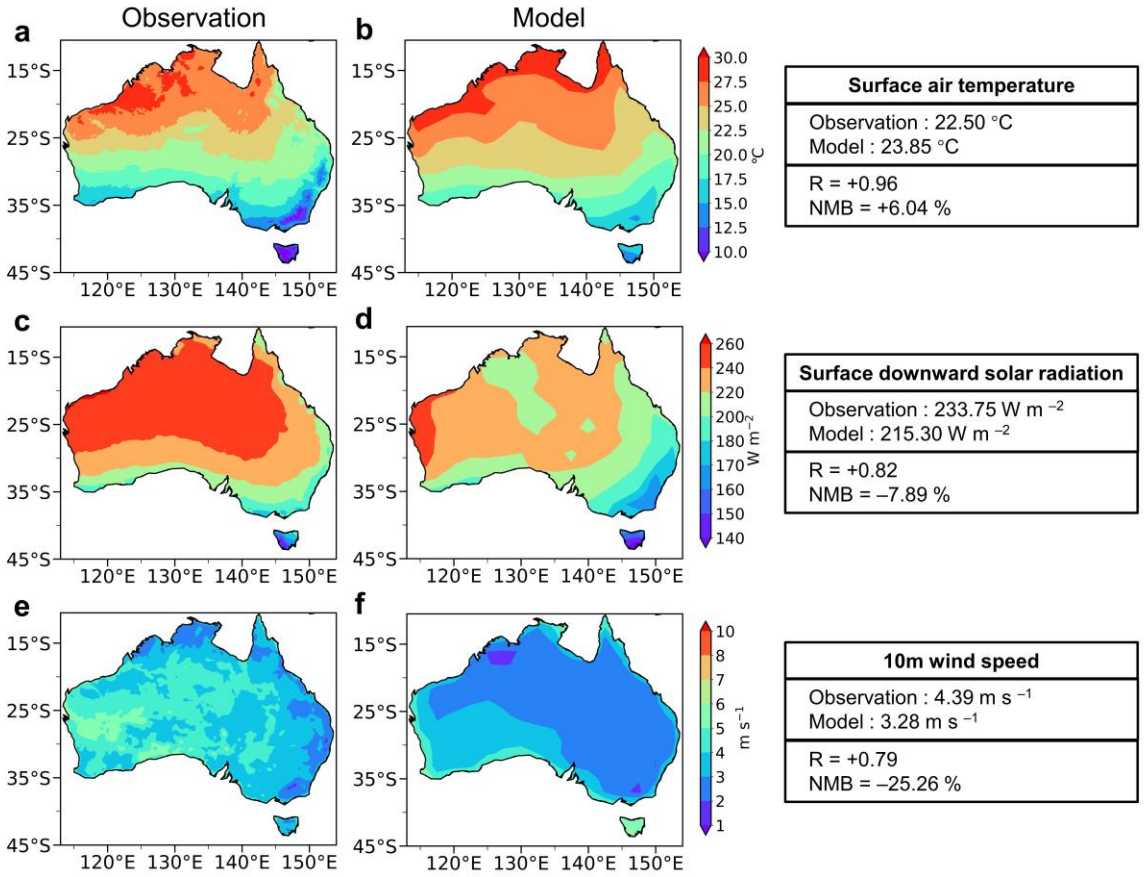

Figure S7. Comparisons of surface air temperature, surface downward solar radiation, and 10m wind speed between observation and model simulation. Same as Figure S4, but for surface air temperature (**a** and **b**, unit: °C), surface downward solar radiation (**c** and **d**, unit: W m^{-2}) and 10m wind speed (**e** and **f**, unit: m s^{-1}).

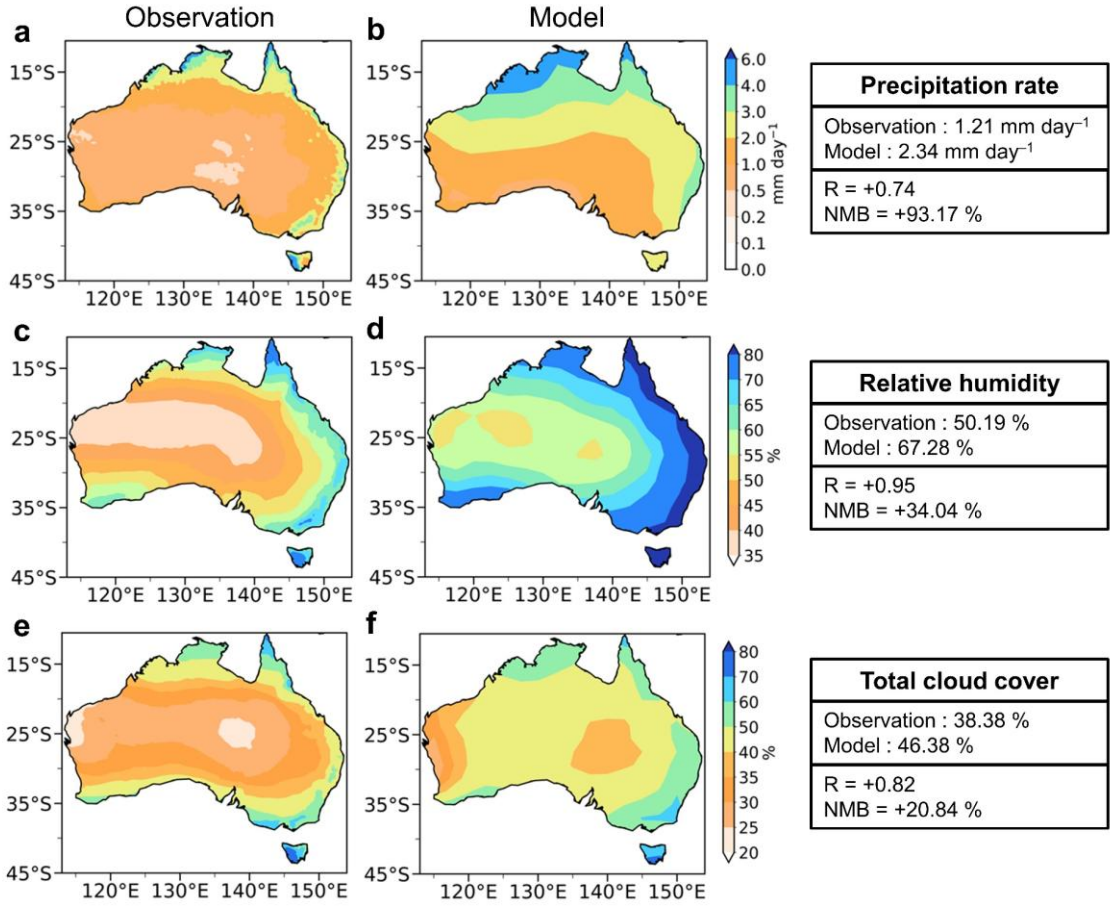

Figure S8. Comparisons of precipitation rate, relative humidity and total cloud cover between observation and model simulation. Same as Figure S4, but for precipitation rate (**a** and **b**, unit: mm day^{-1}), relative humidity (**c** and **d**, unit: %), and total cloud cover (**e** and **f**, unit: %).

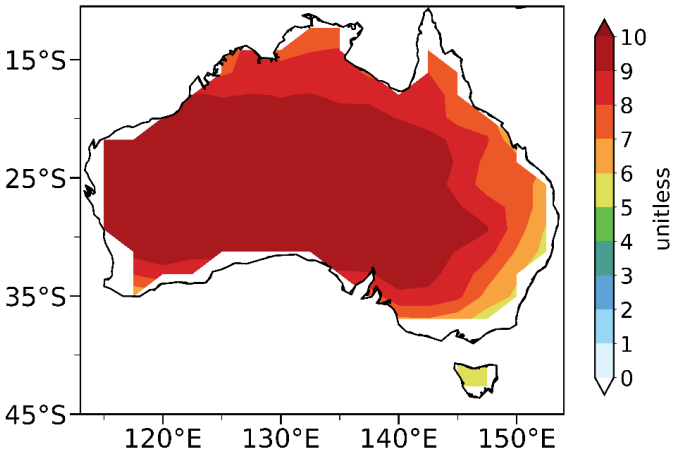

Figure S9. Spatial distributions of annual mean dry factor (unit: unitless) in Australia during 2010–2019. The data is from fire danger indices historical data from the Copernicus Emergency Management Service (CEMS, 2019; Vitolo et al., 2020).

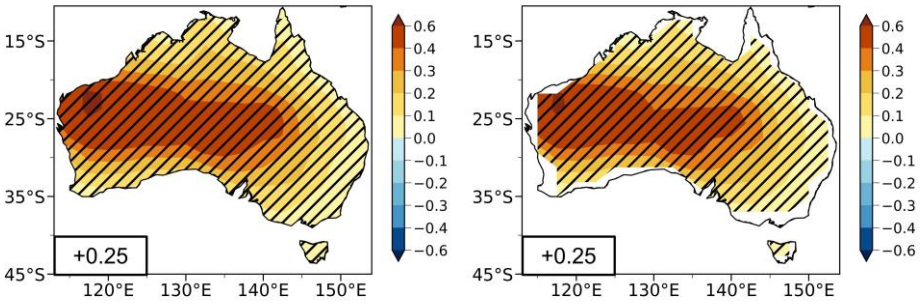

Figure S10. Spatial distribution of simulated changes in FFDI (unit: unitless) during fire seasons in Australia between BASE and CHN (CHN minus BASE). Shaded areas indicate results that are statistically significant at the 90% confidence level. Regional averages for Australia are noted at the bottom-left corner of each panel. The left panel shows FFDI (DF = 10), and the right panel shows FFDI (gridded DF).

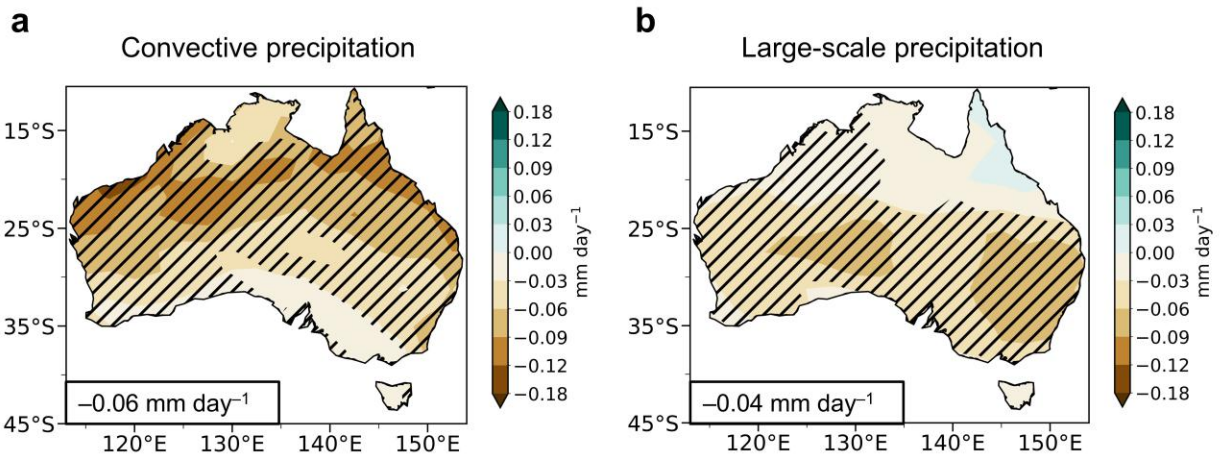

Figure S11. Simulated changes in convective and large-scale precipitation rate in Australia due to aerosol changes in China between 2013 and 2019. Spatial distributions of simulated differences in annual mean convective (**a**) and large-scale (**b**) precipitation rate (unit: mm day^{-1}) in Australia between BASE and CHN (CHN minus BASE). The shaded areas indicate results are statistically significant at the 90% confidence level. Regional averages of the responses over Australia are noted at the bottom-left corner of each panel.

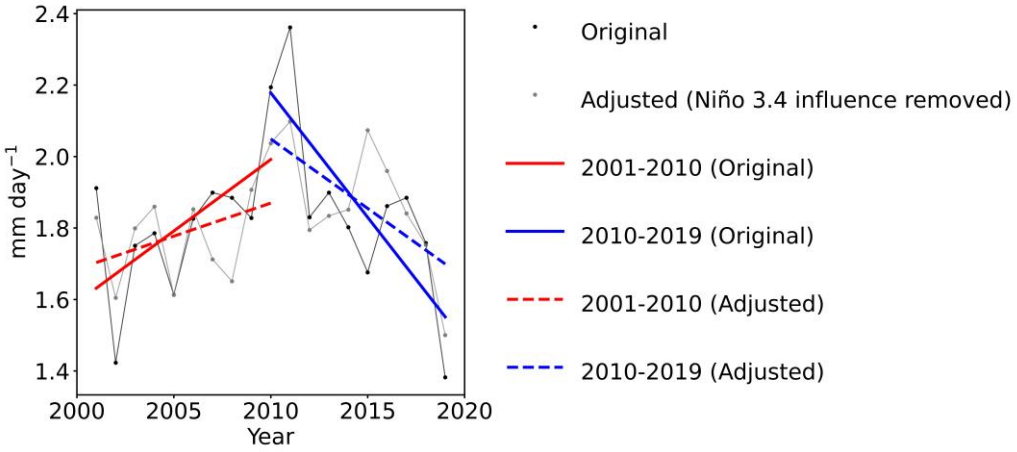

Figure S12. Linear trends of observed precipitation rate during 2001–2019 based on ERA5. The time series of annual mean precipitation rate (unit: mm day^{-1}) over Australia during 2001–2019 from ERA5 reanalysis. The linear trends for the periods 2001–2010 and 2010–2019 are indicated. The time series are also given after removing the influence of Niño 3.4 index.

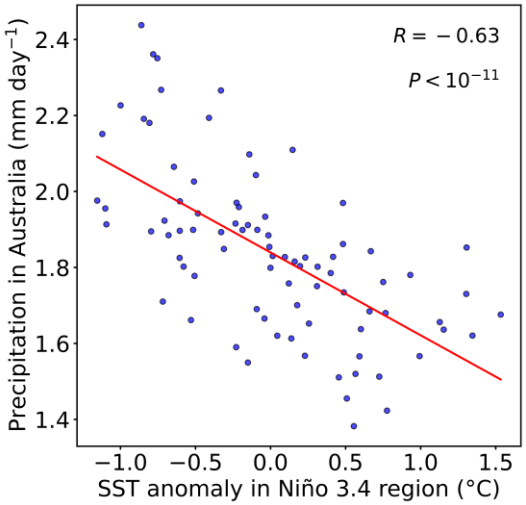

Figure S13. Scatter plot showing the correlation between SST anomaly in Niño 3.4 region and precipitation in Australia. The red line represents the linear regression fit to the data, with the corresponding correlation coefficient (R) and p-value displayed in the figure.

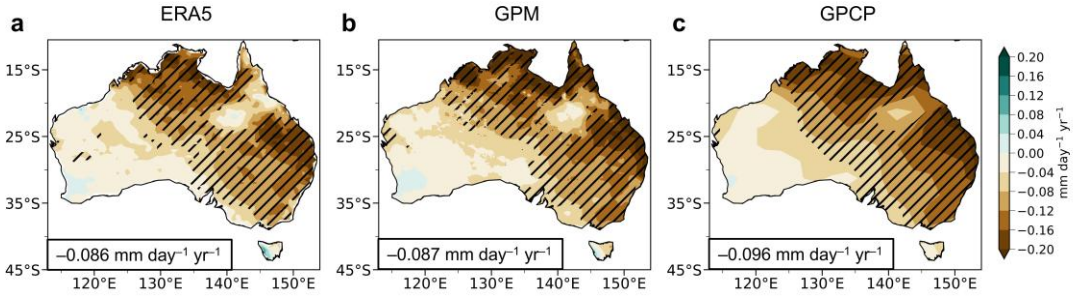

125

126 **Figure S14. Linear trends of observed precipitation rate in Australia based on ERA5,**
127 **GPM, and GPCP.** Spatial distributions of linear trends annual mean precipitation rate (unit: mm
128 day^{-1}) in Australia during 2010–2019 from ERA5 (**a**), GPM (**b**), and GPCP (**c**) datasets. The
129 shaded areas indicate trends are statistically significant at the 90% confidence level. Regional
130 averages over Australia are noted at the bottom-left corner of panels.

131

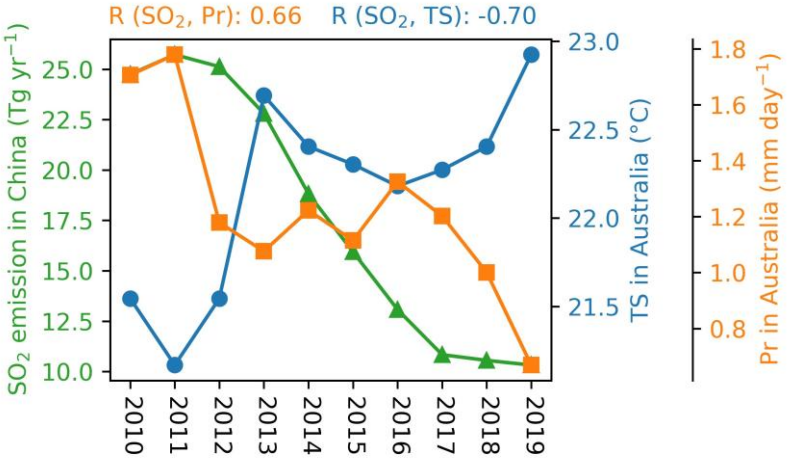

Figure S15. Time series of anthropogenic SO_2 emission in China alongside surface air temperature and precipitation rate averaged over Australia. SO_2 emission (unit: Tg yr^{-1}) data are sourced from CEDS, while surface air temperature (unit: °C) and precipitation rate (unit: mm day^{-1}) data are derived from ERA5. Correlations between SO_2 emission in China and surface air temperature averaged over Australia, as well as between SO_2 emission in China and precipitation rate averaged over Australia, are indicated above the figure.

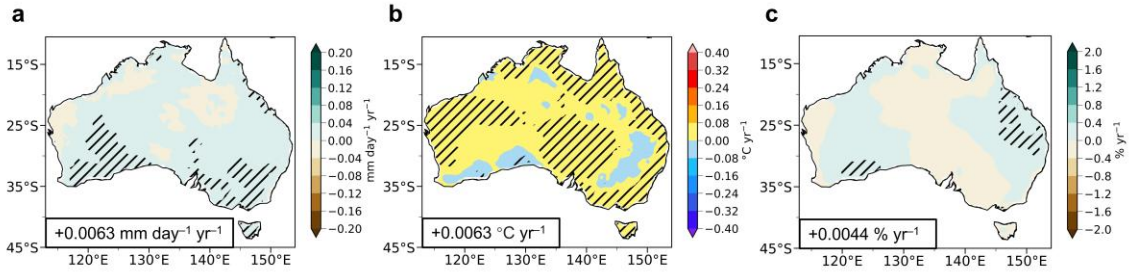

Figure S16. Linear trends of observed precipitation rate, surface air temperature and relative humidity in Australia during 1940–2019 based on ERA5. Spatial distributions of linear trends of annual mean precipitation rate (**a**, unit: mm day^{-1} yr^{-1}), surface air temperature (**b**, unit: °C yr^{-1}) and relative humidity (**c**, unit: % yr^{-1}) in Australia during 1940–2019 from ERA5. The shaded areas indicate trends are statistically significant at the 90% confidence level. Regional averages over Australia are noted at the bottom-left corner of each panel.

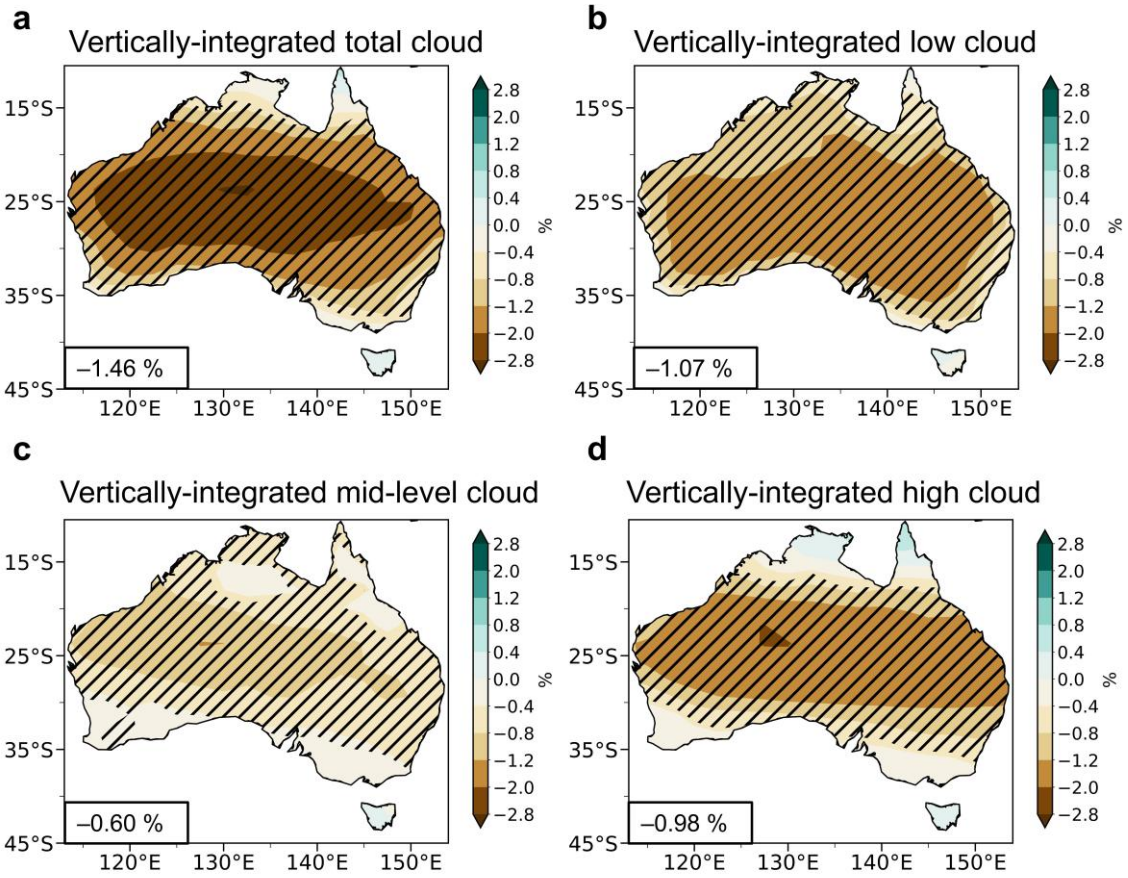

Figure S17. Changes in vertically-integrated total, low, mid-level, and high cloud cover in Australia due to aerosol changes in China between 2013 and 2019. Spatial distributions of simulated differences in annual mean vertically-integrated total (**a**), low (**b**), mid-level (**c**), and high (**d**) cloud cover (unit: %) in Australia between BASE and CHN (CHN minus BASE). The shaded areas indicate results are statistically significant at the 90% confidence level. Regional averages of the responses over Australia are noted at the bottom-left corner of each panel.

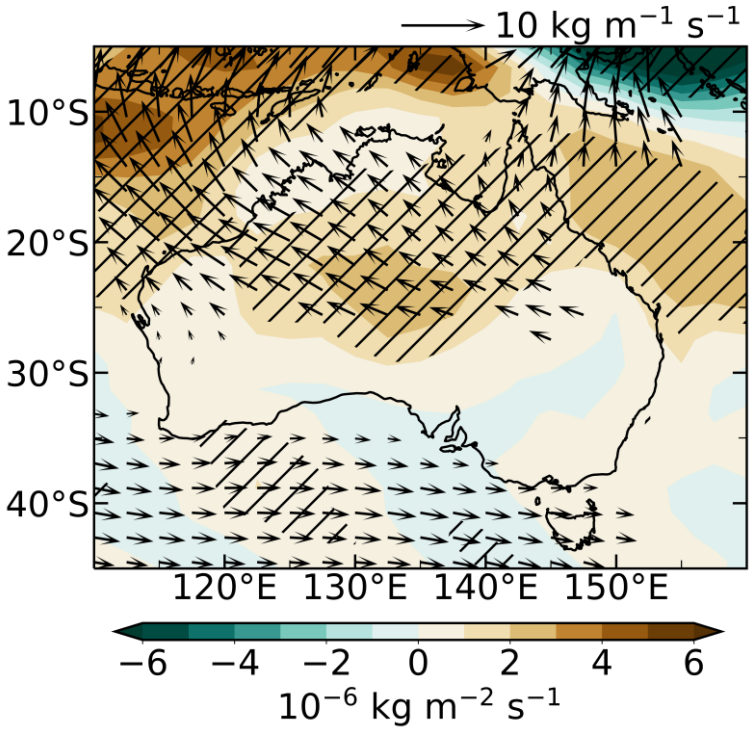

Figure S18. Simulated changes in vertically-integrated moisture flux and its divergence in Australia due to aerosol changes in China between 2013 and 2019. Spatial distributions of simulated differences in annual mean vertically integrated moisture flux (unit: kg m^{-1} s^{-1}, vectors) and its divergence (unit: kg m^{-2} s^{-1}, shades) in Australia between BASE and CHN (CHN minus BASE). Only moisture fluxes which are statistically significant at the 90% confidence level are shown. The shaded areas indicate divergences are statistically significant at the 90% confidence level.

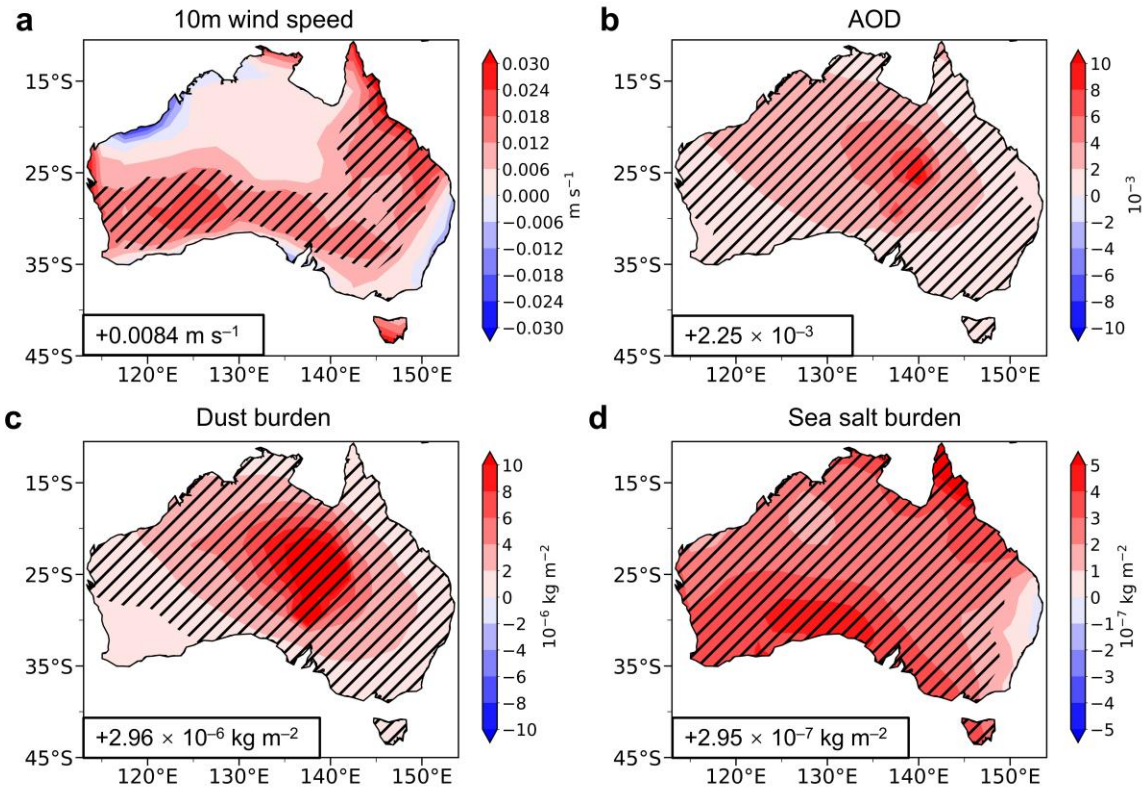

Figure S19. Simulated changes in 10m wind speed, AOD, dust burden, and sea salt burden in Australia due to aerosol changes in China between 2013 and 2019. Spatial distributions of simulated differences in annual mean 10m wind speed (**a**, unit: m s^{-1}), AOD (**b**, unitless), dust burden (**c**, unit: kg m^{-2}), and sea salt burden (**d**, unit: kg m^{-2}) in Australia between BASE and CHN (CHN minus BASE). The shaded areas indicate results are statistically significant at the 90% confidence level. Regional averages of the responses over Australia are noted at the bottom-left corner of each panel.

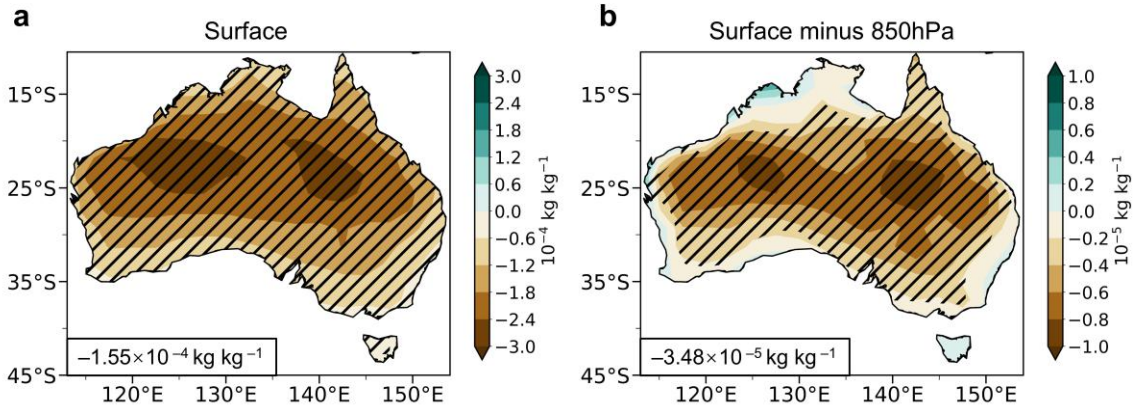

Figure S20. Simulated changes in surface specific humidity and specific humidity differences between surface and 850 hPa in Australia due to aerosol changes in China between 2013 and 2019. Spatial distributions of simulated differences in annual mean surface specific humidity (**a**, unit: kg kg^{-1}) and differences in specific humidity between surface and 850 hPa (**b**, Surface minus 850 hPa, unit: kg kg^{-1}) in Australia between BASE and CHN (CHN minus BASE). The shaded areas indicate results are statistically significant at the 90% confidence level. Regional averages over Australia are noted at the bottom-left corner of each panel.

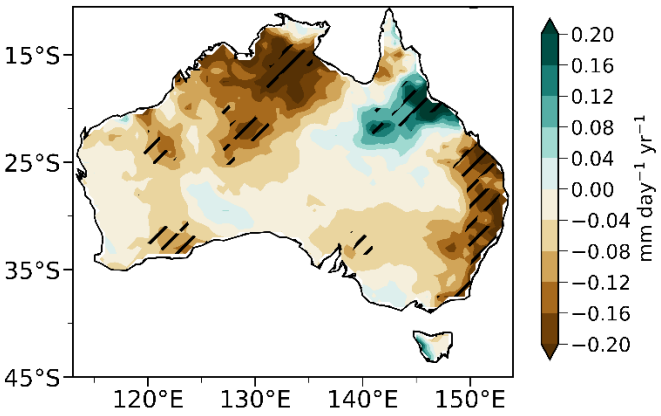

Figure S21. Linear trends of observed precipitation rate in Australia during 2013–2019 based on ERA5. Spatial distributions of linear trends annual mean precipitation rate (unit: mm day^{-1}) in Australia during 2013–2019 from ERA5. The shaded areas indicate trends are statistically significant at the 90% confidence level.

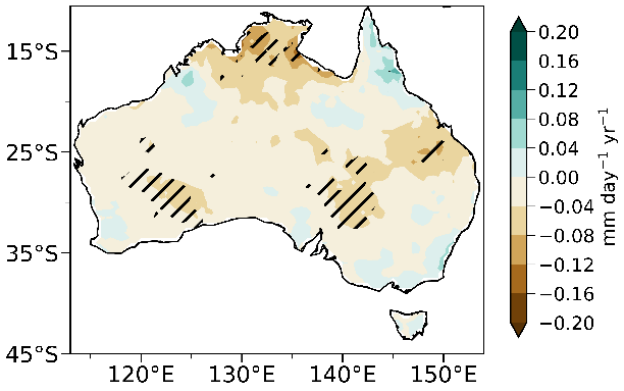

Figure S22. Linear trends of observed precipitation rate in Australia during 2010–2023 based on ERA5. Spatial distributions of linear trends annual mean precipitation rate (unit: mm day^{-1}) in Australia during 2010–2023 from ERA5. The shaded areas indicate trends are statistically significant at the 90% confidence level.

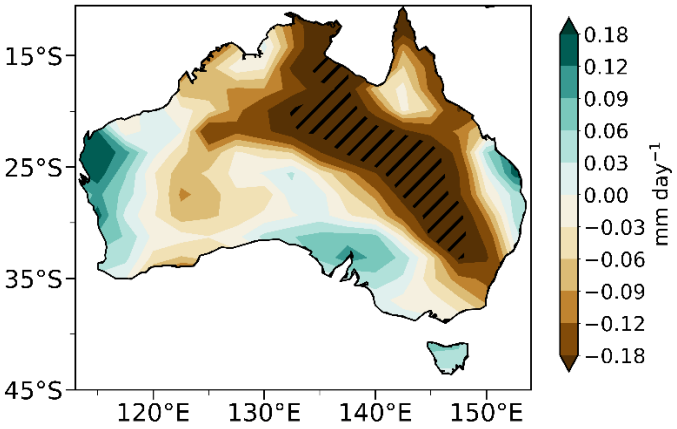

Figure S23. Simulated changes in precipitation rate in Australia due to aerosol changes in China between 2013 and 2019. Spatial distributions of simulated differences in annual mean precipitation rate (unit: mm day^{-1}) in Australia between BASE_FAST and CHN_FAST (CHN_FAST minus BASE_FAST). The shaded areas indicate results are statistically significant at the 90% confidence level. These experiments were run for 30 years, with the last 15 years analyzed using the CESM atmospheric component (CAM5) with fixed sea surface temperature.

205 **References:**

206 CEMS: Fire danger indices historical data from the Copernicus Emergency Management
207 Service, https://doi.org/10.24381/cds.0e89c522, 2019.

208 Vitolo, C., Di Giuseppe, F., Barnard, C., Coughlan, R., San-Miguel-Ayanz, J., Libertá, G., and
209 Krzeminski, B.: ERA5-based global meteorological wildfire danger maps, Sci. Data, 7, 216,
210 https://doi.org/10.1038/s41597-020-0554-z, 2020.